Morphology and Structure of Aerosol Carbon-Encapsulated Metal Nanoparticles from Various Ambient Metal−Carbon Spark Discharges

Jeong Hoon Byeon[†] and Jang-Woo Kim*[,‡]

LCD Division, Samsung Electronics Co., Ltd., Yongin 446-711, Republic of Korea, and Department of Digital Display Engineering, Hoseo University, Asan 336-795, Republic of Korea

ABSTRACT The morphology and structure of aerosol carbon encapsulated metal nanoparticles (CEMNs) of various transition metals (anode; Ti, Cu, Zn, Mo, Pd, W, Pt, or Au) formed by ambient spark discharge at the same electrical operating specifications were analyzed. CEMNs were produced with aggregated carbon particles, and their yields and sizes varied according to the metal-to-carbon fraction of each discharge relating to the ionization potential of the electrode material. Each encapsulated metal had natural crystallinity for all discharges, but carbon graphitization for the Mo−C and W−C configurations, which have relatively small differences in melting temperature between the materials, was particularly weak. An empty zone in the carbon shell was also detected in the CEMNs because of the difference in density between the molten and solid phases of the core metal during encapsulation.

KEYWORDS: carbon-encapsulated metal nanoparticles • morphology • structure • transition metals • ambient spark discharge

Nanomaterials with transition metals and graphitic carbon have attracted considerable interest because of their strong potential for optical and electronic devices, nanoscale storage, catalysis, delivery system, and development of new carbon material s (1–3). The encapsulation of second phases inside carbon shells are of considerable importance in the materials science community. This process not only offers an opportunity to examine dimensionally confined systems but encapsulated materials are also likely to be immune to environmental effects or degradation due to the protective carbon shells surrounding them (4).

Carbon encapsulated metal nanoparticles (CEMNs), which are classified as giant fullerenes due to their outer fullerene-like carbon shells, have attracted considerable attention due to the technological importance stemming from their novel properties (5, 6). In these CEMNs, several-nanometer-thick carbon shells provide chemical stability and protection from the agglomeration of the metal nanoparticles while the nanosized core metal particles can provide specific functions that are unavailable in bulk form. Different metals, such as Fe, Ni, Co, Al, Cu, and Au, have been encapsulated with carbon by a variety of methods, including arc discharge in different atmospheres with a carbon rod as the cathode and a metal or alloy block as the anode (7–11), pyrolysis of carbon materials (12), catalytically assisted chemical vapor deposition (13–15), magnetron and iron-beam cosputtering (16), electron irradiation (17), detonation methods (18), thermal plasma jet (19), flame synthesis (20), and multistep preparation methods using carbon deposition (from the catalytic decomposition of gaseous carbon sources) onto alumina-supported metal particles and then removing the alumina (21, 22). Although each method has both advantages and disadvantages, the high energy and material consumption and intensive hardware of these techniques makes the fabrication of CEMNs rather complex and/or costly (18, 23, 24). In addition, these methods are not mature and require further research and optimization (25).

Being an ambient technique, aerosol synthesis provides a simple and cheap alternative to complex and expensive vacuum synthesis techniques in particle synthesis (26). As one of the aerosol syntheses, spark discharge based on the direct vaporization of a solid precursor material has been used to generate particles of a wide range of conducting materials with sizes ranging from several nanometers up to 100 nm in the aerosol state at ambient temperatures and pressures (27). Recently, carbon encapsulated nanoparticles with iron-group metals (Fe, Co, Ni) were fabricated using a spark discharge reactor as the aerosol synthesis system under ambient conditions (28). As a significant expansion of a previous study (28), this paper reports the ambient spark discharge of metal (anode)−graphite carbon (cathode) configurations to verify the production characteristics of CEMNs from various transition metals (Ti, Cu, Zn, Mo, Pd, W, Pt, or Au). Most effort has been devoted to the encapsulation of iron-group metals within the carbon shells with less work being performed on the above transition metals.

* Corresponding author. Fax: +82-41-540-5925. Tel.: +82-41-540-5929. E-mail: jwkim@hoseo.edu.
Received for review January 7, 2010 and accepted March 11, 2010
[†] Samsung Electronics Co.
[‡] Hoseo University.
DOI: 10.1021/am100015a

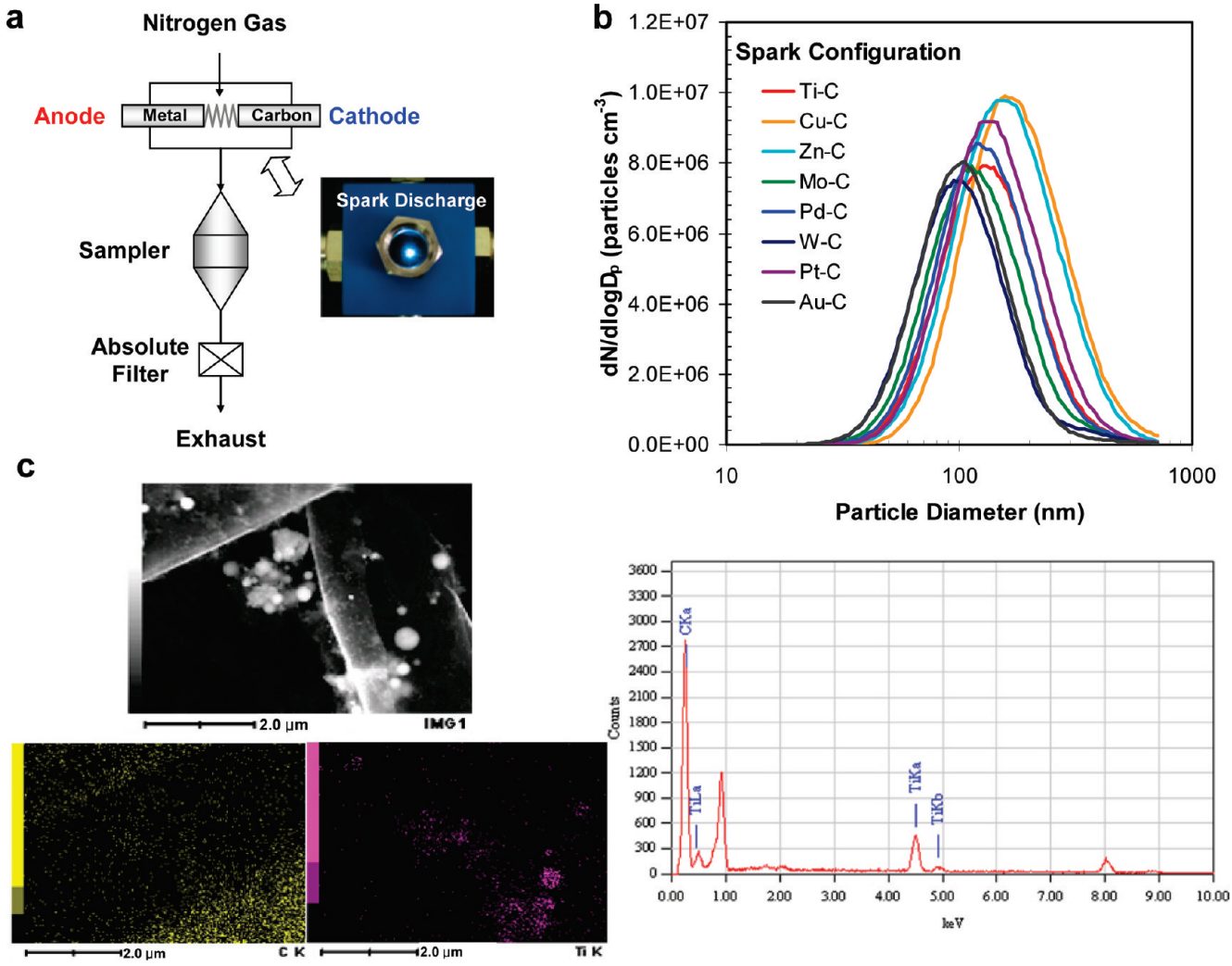

FIGURE 1. (a) Experimental setup of the metal (anode)−carbon (cathode) spark discharge. (b) Size distributions of the spark-produced aerosol particles. (c) SEM image and EDX mapping results (Ti−C configuration).

In the spark discharge apparatus (Figure 1a), a spark channel was formed between a transition metal and graphite rod (each with 3 mm diameter, 100 mm length, Nilaco, Japan) in a chamber under a pure nitrogen (<1 × 10^{-4} impurities) atmosphere at STP. The spark was generated using a current of 2 mA; a voltage drop of 2.0 kV. A frequency of 540 Hz between the electrodes was kept stable by continuously translating the metal rod to the graphite rod to maintain a constant distance (1 mm). The nitrogen gas flow carried the spark produced particles as they exited the spark chamber. The nitrogen gas flow rate was 1 L min^{-1}. The electrical specifications and gas flow rate were different from those reported in a previous study (28) in order to unify the discharge conditions for all configurations. The particle sampling location was 20 cm downstream of the spark discharger. The chamber was cleaned periodically with compressed dry particle-free air to eliminate the residual particles.

Figure 1b shows the size distribution of the spark produced aerosol nanoparticles measured using a scanning mobility particle sizer (SMPS 3936, TSI). Table 1 lists the number concentration (NC), geometric mean diameter (GMD), and geometric standard deviation (GSD) of the particles. Although all the configurations were operated at same electrical specifications, the concentration and size of the produced particles varied according to each configuration. The corresponding metal-to-carbon mass fraction (shown in Table 1) of the spark produced particles was analyzed using inductively coupled plasma-atomic emission spectroscopy (ICP-AES, Perkin-Elmer, Elan 6000) and ranged from 0.14 (Ti−C) to 0.36 (Zn−C). The differences in metal-to-carbon fraction primarily resulted from the spark energy that needed to be delivered in order to evacuate the atom from the crystalline lattice. However, the fractions presented were not matched reasonably to the energy (i.e., operating at same electrical specifications) of the materials, probably because of their heterogeneous spark characteristics, although carbon was the major component for all particles produced. In addition, the highest ionization potential (the energy required to remove of electrons from isolated gaseous atoms, and a higher ionization potential of the material favored atom enrichment) of carbon suggested that it was in the neutral state (29). Therefore, a larger number of carbon atoms than their counter metal atoms could be formed before the formation of solid carbonaceous particles (28).

Table 1. Properties of the Spark-Produced Particles and CEMNs

	anode−cathode configuration							
spark produced particles	Ti−C	Cu−C	Zn−C	Mo−C	Pd−C	W−C	Pt−C	Au−C
metal-to-carbon fraction	0.14	0.23	0.36	0.22	0.25	0.20	0.29	0.31
band area ($I_G/I_{D)}$	0.82	0.80	1.18	0.98	1.02	0.94	0.93	1.03
NC ($\times 10^6$ particles/cm^3)	3.98	5.24	5.34	3.89	4.25	3.63	4.60	3.78
GMD (nm)	132.6	173.2	159.2	117.5	128.6	102.9	140.3	103.0
GSD	1.59	1.61	1.63	1.60	1.59	1.61	1.59	1.57
	anode−cathode configuration							
CEMNs	Ti−C	Cu−C	Zn−C	Mo−C	Pd−C	W−C	Pt−C	Au−C
yield	0.36	0.30	0.66	0.46	0.49	0.42	0.53	0.60
mode diameter (nm)	38.4	46.3	29.9	50.4	58.3	35.3	49.9	32.8
standard deviation	1.25	1.33	1.28	1.28	1.25	1.35	1.22	1.22
t_c/r_m	0.18	0.16	0.38	0.26	0.12	0.28	0.15	0.20
$r_{SolidMetal}/r_0$ measured	0.90	0.91	0.79	0.94	0.92	0.98	0.91	0.88
$r_{SolidMetal}/r_0$estimated	0.93	0.90	0.86	0.95	0.91	0.97	0.93	0.90

Field-emission scanning electron microscopy (FESEM, JSM-6500F, JEOL) (Figure 1c) showed that the sample from the Ti−C configuration, as a representative, was a mixture of spherical particles and aggregates of several primary particles on carbon film support. The difference in brightness of the spherical particles may be due to the difference in secondary electron emission by e-beam irradiation during the SEM operation. In order to verify the elemental composition of the sample, mapping was performed using an energy-dispersive X-ray (EDX, JED-2300, JEOL) spectrometer attached to the SEM (also shown in Figure 1c). The outer region of the spherical particles was carbon and the inner region was titanium. The C K signal was weaker at the inner region of the particles, which is in accordance with a carbon encapsulated metal structure. The C K signals at the other regions matched the aggregates, which mean that they are aggregates of primary carbon particles. These aggregates might have formed from the insufficient metal fraction to be capsulated by carbon; the unreacted carbon (possibly in the molten phase) escaped from the metal−carbon interface and became a solid carbon particle (28).

Raman spectroscopy was used to examine the overall graphitization degree of particles produced. The area intensity ratios (I_G/I_D) between the G and D bands ranged from 1.18 to 0.80 among the samples (Table 1 and the Supporting Information), which originate from individual spectra, indicating the presence of dissimilar graphitization of carbon in each configuration.

The TEM images in Figure 2a revealed the core to be darker (representing a higher density) than that of the shell, which also means that the particle has a metallic core with a carbon shell. The diffraction pattern (inset) was a superposition of two patterns: a set of annular rings originating from graphitic carbon (diffraction from a two-dimensional lattice), and the other spots from a single metallic crystal (arranged in a rectangular lattice). A detailed examination (inset in Figure 2a) of the highly ordered, quasi-spherical, concentric graphitic shells (due to the radial (touching) and tangential (interlocking) growth of carbon plates, giving a "tiled" appearance) shows that, in most cases (except for Mo−C (not shown) and W−C configurations), the carbon lattice fringes (ca. 0.34 nm) can be traced continuously. The final shell state of the CEMNs might be affected by the difference in melting or condensation temperature between the metal and carbon (30). Because the melting points of Mo and W are relatively high, they condense rapidly; so-called "in-between-extremes" character (31) during encapsulation, and the graphitization of the W−C configuration was weaker than that in Mo−C. Moreover, the Zn−C configuration showed the formation of carbon nanotubes (Figure 2b). This suggests that a large (or small) difference resulted in a long (or short) characteristic time to graphitize the carbon atoms on the molten metal surface during cooling by the nitrogen gas flow. On the other hand, the layer distances for cores of Ti−C and Zn−C, Pd−C, and W−C were assigned to the planes of hexagonal-close-packed (hcp), face-centered cubic (fcc), and body-centered cubic (bcc) of metal crystals, respectively, the same trends that were also found in X-ray diffraction (XRD, D/MAX-Rint 2000, Rigaku) analyses (not shown). One possible reason is that a remarkably high ratio ($R_D > 1$) between the diffusivities of the CEMN into the bulk gas (32) and carbon atom into molten metal (33) rarely derived in other crystal phases (e.g., carbides) of the core for all configurations. R_D is calculated using the following equation

$$R_D = 0.67C_c\left(\frac{\Delta T_{c\to g}}{\Delta T_{c\to m}}\right)\left(\frac{\mu_m}{\mu_g}\right)\left(\frac{r_c}{r_p}\right) \quad (1)$$

where $\Delta T_{c\to g}$ and $\Delta T_{c\to m}$ are the temperature in K differentials between the molten carbon and bulk gas and between the molten carbon and molten metal, respectively; μ_m and μ_g are the viscosities in Pa s of the gas ($\sim 1.7 \times 10^{-6}$) and molten metal ($\sim 2-6 \times 10^{-3}$), respectively; and r_c and r_p are the radii in m of the CEMN and carbon atom (7×10^{-11} m), respectively; C_c is the slip correction factor $(1 + (\lambda)/(2r_p)[2.34 + 1.05 \exp(-0.39(2r_p)/(\lambda))]$; λ is the mean free path in m of the gas).

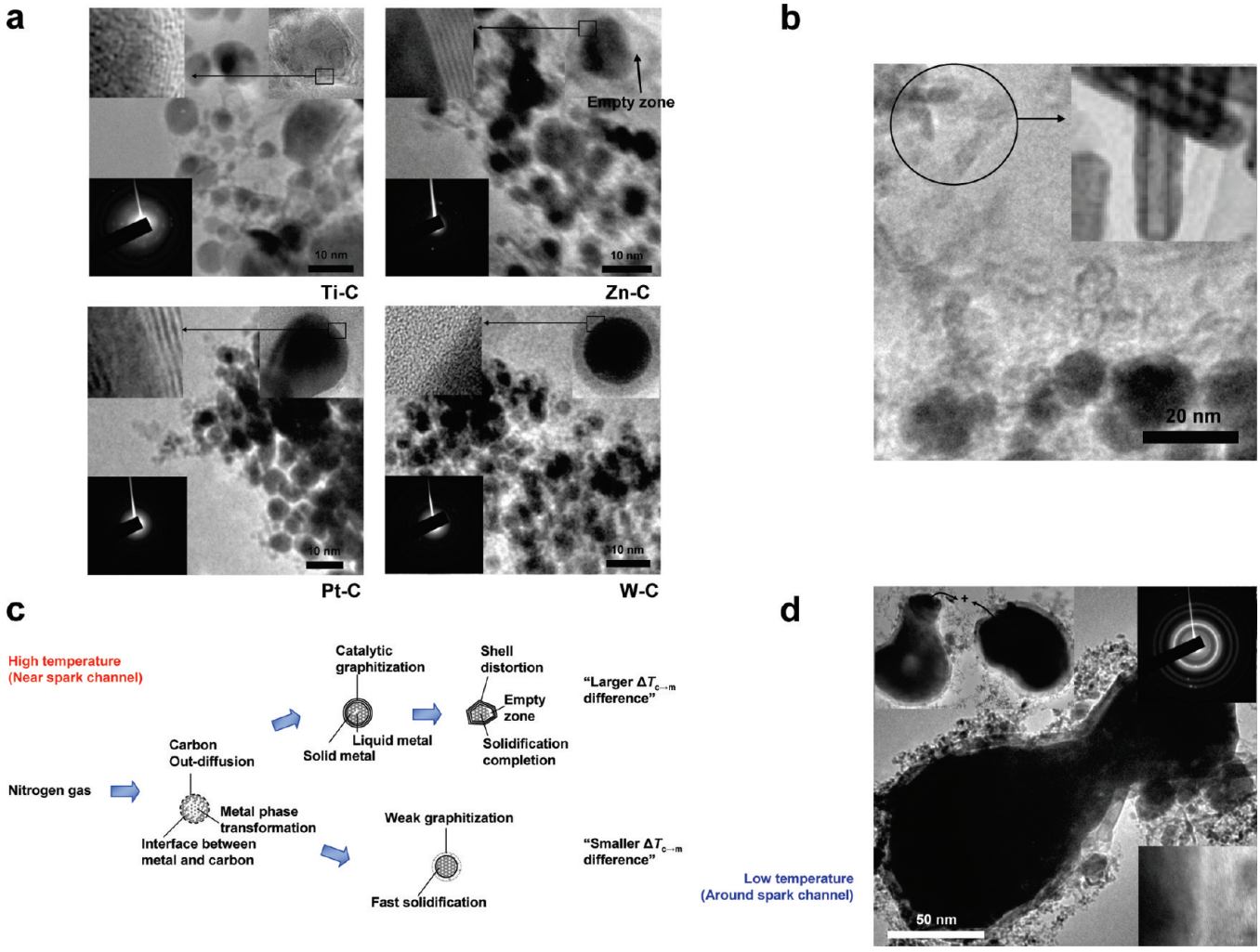

FIGURE 2. (a) TEM image and ED patterns of the CEMNs. (b) Carbon nanotubes from the Zn−C configuration. (c) Mechanism of empty zone formation in a carbon shell. (d) Enlarged CEMN.

Table 1 lists the results and corresponding properties of the CEMNs. The metal-to-carbon ratio plays an important role in the yield of CEMNs and also correlates with their sizes. The yield was determined by the number fraction of the CEMNs (each metallic particle was completely encapsulated by protective carbon shell)-to-all particles in TEM image analyses (~400 particles) with purification steps. The purification steps were as follows: suspending all particles in ethanol under ultrasonication, centrifuging to separate CEMNs and metallic particles from the all particles, drying in air at 323 K. A previous study (28) reported similar trends in that the production yields and sizes of the CEMNs correlated with the metal-to-carbon mass fraction by switching the electrode polarity of the spark. The ratio variations between the thickness (t_c) of the carbon shell and the radius (r_m) of the core metal can be solely or multiply affected by parameters, such as core metal size (34, 35), carbon diffusion to the molten metal surface (36), and defects on the carbon shells (31). There was no correlation between the core metal size and carbon shell thickness because of coupling of the parameters.

Figure 2a also shows an empty zone (insets) between the core and shell of CEMNs. Normally, it is essential that the size of the molten core metal be reduced somewhat by condensation in order to achieve complete encapsulation upon cooling (28). At the end of encapsulation (Figure 2c), the remaining molten metal solidified completely resulting in a decrease in volume. Therefore, an empty zone was formed between the carbon shell and the solid metal core. Gadd et al. (37) estimated the volume change in the molten metal upon solidifying and cooling to room temperature during encapsulation. In this paper, their estimation was modified to examine the in-between-extremes character, and the ratio (shown in Table 1) between the final metal radius of $r_{SolidMetal}$ (298 K) after solidification and a molten radius of r_0 (T_m) was calculated as follows:

$$\frac{r_{SolidMetal(298K)}}{r_0(T_m)} = \left[\frac{\rho_0(T_m)}{\rho_{SolidMetal}(298K)}\right]^{0.33}\left[\frac{T_m}{T_c}\right]^{0.07} \quad (2)$$

where T_m and T_c are the melting temperatures in K of the metal and carbon, respectively; and ρ_0 and $\rho_{SolidMetal}$ are the densities in kg/m^3 of the molten and solid metals, respectively.

Interestingly, when graphitization began on the partially or completely coalesced molten metal particles, the as-

sembled carbon shells shared between multiple particles may drive the particles closer together and accelerate their coalescence (inset), as shown in Figure 2d. More details on the coalescence and subsequent size enlargement of CEMNs are described by Sutter et al. (5, 38).

This technique allows control of the morphological and crystal characteristics of CEMNs using various metal−carbon spark configurations, which will be useful in constructing future carbonaceous nanomaterials in a simple and continuous manner.

Acknowledgment. This research was supported by the Academic Research fund of Hoseo University in 2008 (2008-0023).

Supporting Information Available: Raman spectra of spark produced particles. This material is available free of charge via the Internet at http://pubs.acs.org.

REFERENCES AND NOTES

(1) Kosugi, K.; Bushiri, M. J.; Nishi, N. *Appl. Phys. Lett.* **2004**, *84*, 1753.
(2) Schaper, A. K.; Hou, H.; Greiner, A.; Schneider, R.; Phillipp, F. *Appl. Phys. A: Mater. Sci. Process.* **2004**, *78*, 73.
(3) Tartaj, P.; Morales, M. P.; Veintemillas-Verdaguer, S.; Gonzalez-Carreno, T.; Serna, C. J. *J. Phys. D* **2003**, *36*, R182.
(4) Sun, X.-C.; Reyes-Gasga, J.; Dong, X. L. *Mol. Phys.* **2002**, *100*, 3147.
(5) Sutter, E.; Sutter, P.; Zhu, Y. *Surf. Sci.* **2006**, *600*, 3654.
(6) Kim, J. H.; Kim, C. K.; Kim, Y.-H.; Yoon, C. S. *Colloids Surf., A* **2008**, *321*, 297.
(7) Dravid, V. P.; Host, J. J.; Teng, M. H.; Hwang, B. E. J.; Johnson, D. L.; Mason, T. O.; Weertman, J. R. *Nature* **1995**, *374*, 602.
(8) Ruoff, R. S.; Lorents, D. C.; Chan, B.; Malhotra, R.; Subramoney, S. *Science* **1993**, *259*, 346.
(9) Tsang, S. C.; Chen, Y. K.; Harris, P. J. F.; Green, M. L. H. *Nature* **1994**, *372*, 159.
(10) Sun, X. C.; Nava, N. *Nano Lett.* **2002**, *2*, 765.
(11) Si, P. Z.; Zhang, Z. D.; Geng, D. Y.; You, C. Y.; Zhao, X. G.; Zhang, W. S. *Carbon* **2003**, *41*, 247.
(12) Geng, J.; Jefferson, D. A.; Johnson, B. F. G. *Chem. Commun.* **2004**, *21*, 2442.
(13) Flahaut, E.; Agnoli, F.; Sloan, J.; O'Connor, C.; Green, M. L. H. *Chem. Mater.* **2002**, *14*, 2553.
(14) Wang, Z. H.; Zhang, Z. D.; Choi, C. J.; Kim, B. K. *J. Alloys Compd.* **2003**, *361*, 289.
(15) He, C. N.; Du, X. W.; Ding, J.; Shi, C. S.; Li, J. J.; Zhao, N. Q.; Cui, L. *Carbon* **2006**, *44*, 2330.
(16) Hayashi, T.; Hirono, S.; Tomita, M.; Umemura, S. *Nature* **1996**, *381*, 772.
(17) Ugarte, D. *Chem. Phys. Lett.* **1993**, *209*, 99.
(18) Lu, Y.; Zhu, Z.; Liu, Z. *Carbon* **2005**, *43*, 369.
(19) Bystrzejewski, M.; Karoly, Z.; Szepvolgyi, J.; Kaszuwara, W.; Huczko, A.; Lange, H. *Carbon* **2009**, *47*, 2040.
(20) Grass, R. N.; Athanassiou, E. K.; Stark, W. J. *Angew. Chem., Int. Ed.* **2007**, *46*, 4909.
(21) Tsang, S. C.; Caps, V.; Parakevas, I.; Chadwick, D.; Thompsett, D. *Angew. Chem., Int. Ed.* **2004**, *43*, 5645.
(22) Teunissen, W.; de Groot, F. M. F.; Geus, J.; Stephan, O.; Tence, M.; Colliex, C. *J. Catal.* **2001**, *204*, 169.
(23) Yu, S.-H.; Cui, X.; Li, L.; Li, K.; Yu, B.; Antonietti, M.; Cölfen, H. *Adv. Mater.* **2004**, *16*, 1636.
(24) Kim, J. H.; Kim, J.; Park, J. H.; Kim, C. K.; Yoon, C. S.; Shon, Y. *Nanotechnol.* **2007**, *18*, 115609.
(25) Borysiuk, J.; Grabias, A.; Szczytko, J.; Bystrzejewski, M.; Twardowski, A.; Lange, H. *Carbon* **2008**, *46*, 1693.
(26) Kruis, F. E.; Fissan, H.; Peled, A. *J. Aerosol Sci.* **1998**, *29*, 511.
(27) Borra, J.-P. *J. Phys. D* **2006**, *39*, R19.
(28) Byeon, J. H.; Park, J. H.; Yoon, K. Y.; Hwang, J. *Nanoscale* **2009**, *1*, 339.
(29) Byeon, J. H.; Park, J. H.; Hwang, J. *J. Aerosol Sci.* **2008**, *39*, 888.
(30) Yang, Y.; Liu, X.; Xu, B. *J. Mater. Res.* **2008**, *23*, 1393.
(31) Seraphin, S.; Zhou, D.; Jiao, J. *J. Appl. Phys.* **1996**, *80*, 2097.
(32) Hinds, W. C. *Aerosol Technology*; John Wiley & Sons: New York, 1999.
(33) Mitchell, B. S. *An Introduction to Materials Engineering for Chemical and Materials Engineers*,; John Wiley & Sons: New York, 2003.
(34) Host, J. J.; Teng, M. H.; Elliott, B. R.; Hwang, B. E. J.; Mason, T. O.; Johnson, D. L.; Dravid, V. P. *J. Mater. Res.* **1997**, *12*, 1268.
(35) Jiao, J.; Seraphin, S. *J. Phys. Chem. Solids* **2000**, *61*, 1055.
(36) Rodriguez, N. M. *J. Mater. Res.* **1993**, *8*, 3323.
(37) Gadd, G. E.; Collela, M.; Blackford, M.; Dixon, A.; Evans, P. J.; McCulloch, D.; Bulcock, S.; Cockayne, D. *Carbon* **2001**, *39*, 1769.
(38) Sutter, E.; Sutter, P.; Zhu, Y. *Nano Lett.* **2005**, *5*, 2092.

AM100015A